Configuration improvement for micropressure sensor with vibration interference

Zhongliang Yu, Yulong Zhao, Lili Li, Bian Tian, Rongjun Cheng, Cun Li

State Key Laboratory for Manufacturing Systems Engineering, Xi'an Jiaotong University, Xi'an, Shaanxi 710049, People's Republic of China
E-mail: zhaoyulong@mail.xjtu.edu.cn

Published in Micro & Nano Letters; Received on 8th May 2014; Revised on 4th July 2014; Accepted on 1st September 2014

Presented is the configuration design for piezoresistive absolute micropressure sensors. A figure of merit called the performance factor (PF) is defined as a quantitative index to describe the comprehensive performances of a sensor including sensitivity, resonant frequency and acceleration interference. Two configurations are proposed through introducing islands and sensitive beams into the typical flat diaphragm. The stress distributions of sensitive elements are analysed by a finite element method. Multivariate fittings based on ANSYS simulation results are performed to establish the equations on surface stresses and deflections of the two sensors. Optimisation by MATLAB is carried out to determine the dimensions of the configurations. Convex corner undercutting is analysed to estimate the final dimensions of the islands. Each PF of the two configurations with the determined dimensions has been calculated and compared. Silicon bulk micromachining is utilised to fabricate the prototypes of the sensors. The outputs of the sensors under both static and dynamic conditions are tested. Experimental results reveal that the configuration with quad islands presents the highest PF of 210.947 $Hz^{1/4}$. The favourable overall performances make the sensor more suitable for altimetry.

1. Introduction: With the further development of aerospace engineering, a number of piezoresistive pressure sensors are desired for micropressure measurements. According to the relationship between pressure and height, the aircraft altimetry can be obtained through measuring pressure. Owing to the extremely low pressure at high altitude, high sensitivity is needed to ensure the accuracy of orbital correction. A high overload resistance is also required for a micropressure sensor to bear the atmosphere on the earth. To develop a micropressure sensor with high sensitivity and overload resistance is important and a necessity for aerospace. Moreover, the vibration interference should be taken into account to improve the accuracy of pressure measurements. To some degree the chip configuration determines the sensitivity, overload resistance and dynamic properties [1–4]. The lower the pressure range, the thinner the diaphragm needed to maintain high sensitivity. However, an excessively thin membrane may induce large deflection and instability, leading to unfavourable performances of a sensor such as linearity, resonant frequency, safety factor etc. [5]. Therefore, the configuration design of a sensor chip is critical.

Improvements in sensing configuration design have made the performances of sensors better. Shimazoe *et al.* [6] developed a sensor with a centre boss on the diaphragm and an annular groove formed on the back surface of the diaphragm. Although the accuracy was 0.17% full scale (FS), variation of stress distribution was evident, thus the high precision placement of piezoresistors was demanded. Moreover, the sensor was unfavourable to miniaturisation and batch production. Bao *et al.* [7] proposed a beam-diaphragm configuration by introducing beams on the flat membrane of a twin isles configuration, forming a shape like a dumbbell. The nonlinearity of 0.25% FS was relatively low, but the sensitivity of 0.6901 μV/V/Pa was slightly lower for the measuring range of 1 kPa, and the overload resistance was lower because of the lack of thick islands in the rear cavity. Johnson *et al.* [8] reported a novel ribbed and bossed configuration. The incorporation of a rib into the diaphragm for stress concentration was proved to be effective in enhancing sensitivity and reducing deflection. In addition, the introduction of a self-aligning rim was favourable for enhancing the manufacture. However, the overload resistance was a bit lower because of the thin bosses. Tian *et al.* [3] designed a beam-membrane configuration through etching a crossbeam on the flat diaphragm, resulting in a good linearity (the nonlinearity was 0.09% FS) for the measurements of 5 kPa, while the overload resistance and the sensitivity of 1.549 μV/V/Pa were relatively low.

To measure the absolute micropressure, both high sensitivity and high overload resistance are required. As the existing design schemes discussed fail to fully meet the requirements, two configurations are put forward for the measuring range of 500 Pa. By incorporating beams into the diaphragm, stresses are expected to be concentrated. High overload resistance is anticipated because of the introduction of islands to limit the displacement. However, the introduction of islands will make the vibration interference protrude. Therefore, taking the vibration influences into account is critical for improving the accuracy of micropressure sensors under dynamic conditions. A performance factor (PF) involving sensitivity, resonant frequency and acceleration interference is established to try to reflect the overall performance of a sensor. To choose the optimal configuration with high sensitivity, high bandwidth and low vibration interference, a general optimisation method is proposed. As no theoretical formula needs to be derived, the method can be widely applied rather than limited to the configuration discussed in this Letter. The advantages are obvious, especially when the theoretical formula is hard to be deduced. By converting the nonlinear problem into linear, the configuration optimisation is much more efficient.

2. Definition of PF: As absolute micropressure sensors always have to be exposed to the atmosphere, the introduction of islands is indispensable for withstanding the high overload. However, the introduced mass decreases the natural frequency of a configuration and increases the acceleration interference. To describe the comprehensive performances of a sensor including sensitivity, resonance frequency and acceleration interference, a figure of merit called the performance factor is defined as a quantitative assessment

$$\mathrm{PF} = \mathrm{SNR} \cdot \sqrt[4]{f} = \frac{U_{\mathrm{fp}}}{U_{\mathrm{fa}}} \cdot \sqrt[4]{f} \tag{1}$$

where PF is the performance factor. U_{fp} and U_{fa} are the full-scale output voltages under pressure and acceleration interference applied, respectively. SNR is the signal-to-noise ratio defined as

doi: 10.1049/mnl.2014.0236

U_{fp}/U_{fa}. f is the resonant frequency and the fourth root of it is extracted to make the effect weight between f and SNR in the same order of magnitude. The relationship between full-scale output and stress can be expressed as follows (take the resistor oriented in the ⟨110⟩ direction on a (100) n-type silicon wafer for example) [9, 10]

$$U_f \simeq \frac{1}{2}\pi_{44}(\sigma_x - \sigma_y)U_i \tag{2}$$

where U_f is the full-scale output voltage, U_i is the input voltage and π_{44} is the shear piezoresistance coefficient. σ_x and σ_y are the longitudinal and transversal surface stress at the central point of a resistor. The full-scale output U_f can also be expressed as

$$U_f = S \cdot R \cdot U_i \tag{3}$$

where S is the sensitivity and R is the measuring range. Based on (2) and (3), the SNR can be written as

$$\mathrm{SNR} = \frac{U_{fp}}{U_{fa}} \simeq \frac{\sigma_{dp}U_{ip}}{\sigma_{da}U_{ia}} = K_1\frac{\sigma_{dp}}{\sigma_{da}} \tag{4}$$

$$\mathrm{SNR} = \frac{U_{fp}}{U_{fa}} = \frac{S_pR_pU_{ip}}{S_aR_aU_{ia}} = K_1K_2\frac{S_p}{S_a} \tag{5}$$

where σ_{dp} and σ_{da} are the difference of longitudinal and transversal surface stress at the centre of a resistor under pressure and acceleration interference applied, respectively. S_p, S_a; R_p, R_a; U_{ip}, U_{ia} are the sensitivity, measuring range and input voltage under the pressure and acceleration interference exerted separately, respectively. K_1 is defined as U_{ip}/U_{ia}, and usually the input voltage U_{ip}, U_{ia} are equal, so K_1 is 1. K_2 is defined as R_p/R_a. Since the measuring ranges R_p and R_a are 500 Pa and 15 g in this investigation, K_2 can be calculated as 3.4. Namely, both of the K_1 and K_2 can be regarded as constant here. According to (4) and (5), the PF in (1) can be rewritten as

$$\mathrm{PF} = \frac{U_{fp}}{U_{fa}}\cdot\sqrt[4]{f} = K_1K_2\frac{S_p}{S_a}\cdot\sqrt[4]{f} \simeq K_1\frac{\sigma_{dp}}{\sigma_{da}}\cdot\sqrt[4]{f} \tag{6}$$

The defined PF in (6) is favourable to reflecting an overall performance including sensitivity and dynamic properties.

3. Configuration analysis

3.1. Configuration establishment: Since absolute micropressure sensors have to bear the atmosphere on the earth, which is hundreds of times higher than the measuring range, the silicon configuration can be easily fractured under such a high overload. In view of the situation, the typical bossed-diaphragm (E-type) configuration should be taken into account. Owing to the mass bulk support, the membrane may withstand atmosphere without breaking. However, the introduction of mass bulk partly sacrifices the effective stress that reflects sensitivity, and makes the sensor sensitive to the vibration interfering signal. In an attempt to increase the sensitivity, bandwidth and decrease the dynamic interfering signal, two configurations, namely beam-membrane-mono-island (BMMI) and beam-membrane-quad-island (BMQI) configurations, are presented as shown in Fig. 1. Sensitive beams are located on the membrane, and islands are placed in the rear cavity.

3.2. Configuration optimisation: To optimise and determine the configuration dimensions, formulas need to be established. Because of the existence of beams on the membrane, theoretical formulas are difficult to derive, while approximate ones can be

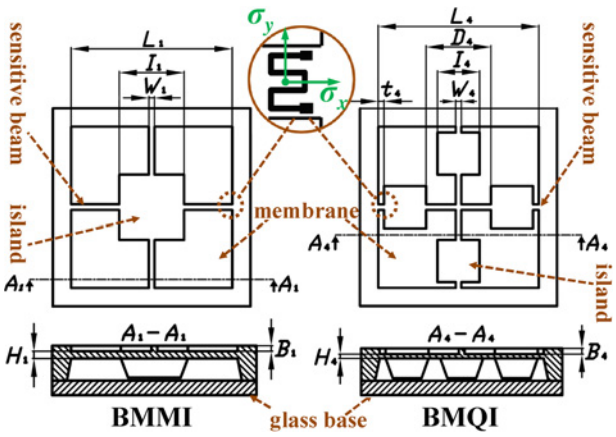

Figure 1 *Front and cross-sectional views of the two structures*

drawn by the combination of finite element method (FEM) calculation and multivariate fitting.

For convenience of illustration, the front views and the cross-sectional views in Fig. 1 are marked with dimension variables. L_1 and L_4 refer to the effective width of membranes; H_1 and H_4 are the thickness of membranes; I_1 and I_4 are the top width of islands; D_4 is the distance of two opposite islands; W_1 and W_4 are the width of beams; B_1 and B_4 are the thickness of beams; t_4 is the length of sensitive beams. The numbers 1 and 4 in the subscripts of variables represent the BMMI and BMQI configurations, respectively, and this principle applies throughout.

The mechanical stress and the maximum deflection of the typical flat diaphragm configuration are the power functions of each variable [11]. Similarly, the functional forms of the two configurations might be the same. The differential stress of BMMI is assumed as follows

$$\sigma_{dp1} = K \cdot B_1^a \cdot H_1^m \cdot I_1^n \cdot L_1^r \cdot W_1^s \tag{7}$$

where σ_{dp1} is the difference of x and y direction stress at the centre of a resistor (as shown in Fig. 1) when a 500 Pa pressure applied. B_1, H_1, I_1, L_1 and W_1 are the independent dimension variables chosen from the variables described above; K, a, m, n, r and s are the undetermined constants. To ascertain the constants, the variation of σ_{dp1} with variables should be studied by ANSYS loop computation using the standard (100) silicon wafer material properties described in [12]. In the calculation, three values for each variable are assigned. Therefore, 243 loops are needed to cover the entire variable space. Based on the results, multivariate fitting by MATLAB is carried out. For the simplification, nonlinear fitting is transformed to linear via taking the logarithm of (7)

$$\begin{aligned}\ln(\sigma_{dp1}) = \ln(K) + a\cdot\ln(B_1) + m\cdot\ln(H_1)\\ + n\cdot\ln(I_1) + r\cdot\ln(L_1) + s\cdot\ln(W_1)\end{aligned} \tag{8}$$

The parameters after the logarithm can be regarded as new variables. Hence, a multiple linear regression problem that costs much less is raised and easily solved. To obtain the constant K in (7), a natural exponential of the constant item $\ln(K)$ in (8) should be taken into account. The fitted equation concerning the differential stress σ_{dp1} is obtained

$$\sigma_{dp1} = 39.48159\frac{L_1^{3.40878}}{B_1^{0.52501}H_1^{1.40483}I_1^{0.67321}W_1^{0.611}} \tag{9}$$

Since the values of deflection have been calculated by ANSYS in the same cycles, the equation deflection is established based on

MATLAB fitting as stated above

$$\omega_1 = 1.41092 \times 10^{-12} \frac{L_1^{6.46809}}{B_1^{1.0975} H_1^{1.7941} I_1^{1.99602} W_1^{0.44098}} \quad (10)$$

where ω_1 is the maximum deflection of BMMI at the centre of the membrane under the pressure of 500 Pa. In the same way, namely by the combination of ANSYS loop calculation and MATLAB fitting, the equations of BMMI concerning the overload and dynamic conditions are established, respectively

$$\sigma_{\text{overload1}} = 7.88531 \times 10^{6} \frac{B_1^{0.19031} I_1^{0.6139}}{H_1^{0.01866} L_1^{1.39303} W_1^{0.25704}} \quad (11)$$

$$\sigma_{\text{da1}} = 1.43370 \times 10^{2} \frac{L_1^{2.20622} I_1^{0.63011}}{B_1^{0.45818} H_1^{1.29155} W_1^{0.59079}} \quad (12)$$

$$f_1 = 1.01868 \times 10^{6} \frac{B_1^{0.52675} H_1^{0.84985} I_1^{0.36098} W_1^{0.21553}}{L_1^{2.66285}} \quad (13)$$

where $\sigma_{\text{overload1}}$ is the maximum von Mises stress under an atmospheric pressure of 100 kPa. σ_{da1} is the difference of x and y direction stress at the centre of a resistor under a 15 g acceleration applied in the normal direction of the membrane. f_1 is the resonant frequency.

To validate the rationality of the hypothesis regarding the functional forms established in (9)–(13), their coefficients of determination R^2 are calculated to verify the goodness of fit. The values are 0.96793, 0.98129, 0.97664, 0.96261 and 0.97572 successively, which demonstrate the fittings are good, thus the ANSYS simulation results can be almost represented by these equations. The performance factor PF_1 can be obtained by plugging σ_{dp1}, σ_{da1} from (9) and (12) into (6)

$$\text{PF}_1 = 8.74875 \frac{B_1^{0.06486} H_1^{0.09918} L_1^{0.53685} W_1^{0.03367}}{I_1^{1.21308}} \quad (14)$$

In the same manner, the equations on BMQI can be deduced

$$\sigma_{\text{dp4}} = 42.85568 \frac{L_4^{3.24387}}{B_4^{0.72821} H_4^{1.24559} I_4^{0.14835} W_4^{0.69285} t_4^{0.17902}} \quad (15)$$

$$\omega_4 = 4.65594 \times 10^{-11} \frac{L_4^{4.39870}}{B_4^{1.33615} H_4^{1.54480} I_4^{0.14935} W_4^{0.54189} t_4^{0.38890}} \quad (16)$$

$$\sigma_{\text{overload4}} = 1.85745 \times 10^{6} \frac{B_4^{0.26293} H_4^{0.19110} I_4^{0.06102} L_4^{0.01517}}{W_4^{0.14454} t_4^{1.28317}} \quad (17)$$

$$\sigma_{\text{da4}} = 1.39505 \times 10^{4} \frac{I_4^{1.70689} L_4^{1.32893} t_4^{0.00859}}{B_4^{0.55853} H_4^{1.02505} W_4^{0.64087}} \quad (18)$$

$$f_4 = 1.35776 \times 10^{4} \frac{B_4^{0.5754} H_4^{0.62839} W_4^{0.21864}}{I_4^{0.91863} L_4^{1.08254} t_4^{0.31316}} \quad (19)$$

$$\text{PF}_4 = 3.31608 \times 10^{-2} \frac{L_4^{1.64431} W_4^{0.00268}}{B_4^{0.02583} H_4^{0.06344} I_4^{2.0849} t_4^{0.2659}} \quad (20)$$

The coefficients of determination R^2 for (15)–(19) are 0.96686, 0.978214, 0.98751, 0.97484 and 0.98308. The variables, σ_{dp4}, ω_4, $\sigma_{\text{overload4}}$, σ_{da4}, f_4, PF_4 have the same meanings as stated in the BMMI-related equations. The numbers in subscripts are used for the discrimination of different configurations as stated above. During the establishment of equations for BMQI, three values for each variable are assigned as well, thus 729 loops are needed to involve the whole variable space. Specifications about the equations discussed are that the ranges of all the variables are constrained by actual demands.

The international system of units is adopted throughout.

To search for the optimal overall performances, configuration optimisation models are established and listed in Table 1, where the unit micrometre is adopted for dimension variables. In the Table, σ_b is the ultimate strength of single crystal silicon, n_1, n_4 the safety factors. According to the small deflection theory, the nonlinearity below 1% FS can be achieved if the maximum deflection of the flat diaphragm is kept under one-fifth of the film thickness [13]. For rough reference, the same evaluation of maximum deflection as a constraint is employed in the models. By taking the natural logarithms of objective functions and constraints, equivalent linear optimisation problems that apparently simplify computation are raised. MATLAB is used to search for the optimal solutions of the two configurations, and the value of dimension variables is got by taking natural exponentials of the optimisation results.

Under the given constraints and safety factors in Table 1, the sizes of the configurations are determined. The two configurations feature the identical 7000 μm × 7000 μm overall dimensions, 20 μm thickness membranes, 200 μm width and 30 μm thickness beams. The lengths of the sensitive beams are 1700 and 200 μm and the top widths of the islands are 2300 and 1500 μm corresponding to BMMI and BMQI. The uniform configuration dimensions are acquired by adjusting the constraints and safety factors in Table 1, which makes it convenient for PF comparison later. Certainly, the constraints and safety factors can be modified according to the specific optimisation situations.

3.3. Convex corner (CC) undercutting estimation: Under the determined dimensions above, the islands of BMQI are lacking enough space for compensation, thus CC undercutting occurs. The final dimensions of the islands are roughly estimated using the fast etching planes described in [14], to which the etching concentration and temperature have been referred. For simplification, the fast etching planes are assumed as {4 1 1} all the time. According to the literature, the etching depth is 0.544 times the side length of the compensation structure. Based on the relationship, the etching depth when the compensation structure is consumed can be calculated. h_{41}, representing the midway etching depth of BMQI, is 108.8 μm. By this time, complete corners have formed simultaneously on both of the bottom and midway root planes of the islands. Points $A_{40\text{m}}$ and $A_{41\text{m}}$ represent the vertices of the corners on the bottom and midway root planes as shown in Fig. 2*a*. This moment $A_{40\text{m}}A_{41\text{m}}$ coincided with the intersection lines of the {1 1 1} planes. With the etching going on, $A_{40\text{m}}A_{41\text{m}}$ will move parallel to these intersection lines, although the corners are undercut by the

Table 1 Optimisation models about the performance factors of geometries

BMMI	BMQI
$\max(\text{PF}_1)$	$\max(\text{PF}_4)$
subject to	subject to
$20 \le B_1 \le 30$	$30 \le B_4 \le 50$
$10 \le H_1 \le 20$	$20 \le H_4 \le 30$
$2300 \le I_1 \le 3000$	$1500 \le I_4 \le 1600$
$5000 \le L_1 \le 5700$	$5000 \le L_4 \le 5700$
$100 \le W_1 \le 200$	$100 \le W_4 \le 200$
$\omega_1 \le 0.2H_1$	$100 \le t_4 \le 400$
$\sigma_{\text{overload1}} \le \sigma_b/n_1$	$\omega_4 \le 0.2H_4$
$\sigma_b = 7$ Gpa	$\sigma_{\text{overload4}} \le \sigma_b/n_4$
$n_1 = 15$	$\sigma_b = 7$ Gpa
	$n_4 = 4$

doi: 10.1049/mnl.2014.0236

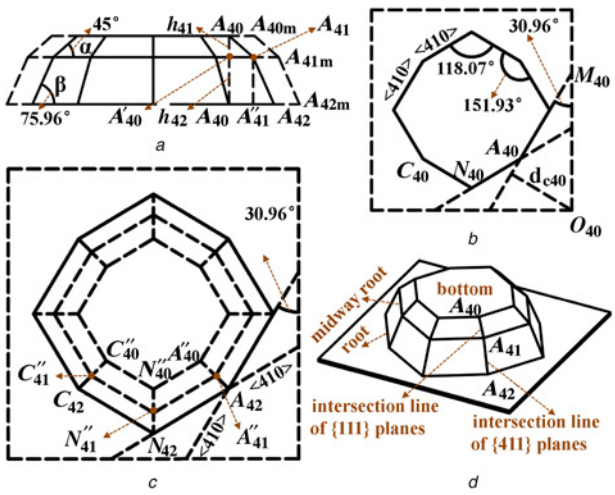

Figure 2 *Analysis and calculation model about CC undercutting of BMQI*
a Side view of the undercutting process
b Top view of the undercutting process on the bottom plane
c Top view of the undercutting process on the root plane
d Estimated island model after CC undercutting

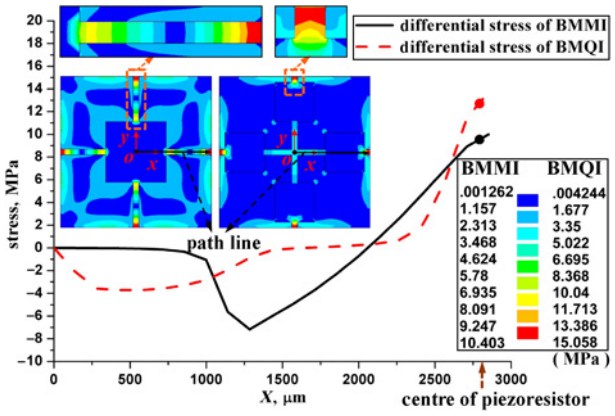

Figure 3 *Simulation results about stress distribution and stress path*

etching front lines in the ⟨4 1 0⟩ directions. This is because the corners from the bottom to the midway root are exposed for the same etching time. As for the corners from the midway root plane to the final root plane, they will be undercut by the {4 1 1} planes. That is, the vertices of the corners on the midway root and final root planes are always on the intersection lines of the {4 1 1} planes.

In Fig. 2*a*, the points A_{40}, A_{41} and A_{42} represent the final vertices of the corners on the bottom, midway root and final root planes, respectively. A'_{40} are A''_{40} are the projection of A_{40} on the midway root and final root planes, respectively. h_{42}, the etching depth between the midway root and final root planes, is 241.2 μm, because of the total etching depth of 350 μm. α, the angle between the line of $A_{40}A_{41}$ and the {1 0 0} planes, is 45° and β, the angle between the line of $A_{41}A_{42}$ and {1 0 0} planes, is 75.96°. According to the conditions, the length of $A_{41}A'_{40}$, $A_{42}A''_{40}$ can be calculated.

In Fig. 2*b*, d_{c40} is the vertical distance from points O_{40} to the etching front lines $A_{40}M_{40}$, and it can be calculated by multiplying h_{42} with 1.46 on the basis of [14]. According to the geometrical relationship shown in Fig. 2*b*, $C_{40}N_{40}$, the side length of the island bottom is 284 μm. Based on the bottom dimensions and the length of $A_{41}A'_{40}$, $A_{42}A''_{40}$ calculated above, the dimensions of the midway root and the final root of the island can be calculated. In Fig. 2*c*, $C''_{41}N''_{41}$, the side length of the midway root, is 373 μm, and $C_{42}N_{42}$, the side length of the final root, is 423 μm. The estimated island model after CC undercutting is presented in Fig. 2*d*.

3.4. Performance evaluation: To evaluate the performances of the two sensors with the calculated dimensions (considering the influence of CC undercutting), ANSYS is used. The simulation results on the distribution of von Mises stress on sensitive beams and the stress path along the *x*-axis from the centre to the edge of sensitive beams under the pressure of 500 Pa are shown in Fig. 3.

To assess the influence of vibration on pressure measurements, both acceleration analysis and modal analysis are carried out. In the simulation for acceleration analysis, a maximum acceleration of 15 g is exerted because of the human extreme limit.

Both of the static and dynamic analysis results above are listed in Table 2. In addition, the E-type is analysed as well. For obvious comparison, the dimensions of the E-type are equal to the ones of BMMI except for the beam. In the Table, U_{fp} and U_{fa} represent the full-scale outputs under the pressure and the acceleration applied, respectively. The f represents the resonant frequency. The full-scale outputs on pressure and acceleration are derived by (2) based on the simulated differential stress. In this Letter, the concentration of ion implantation is 3×10^{14} cm^{-3}, less than 1×10^{17} cm^{-3}, so π_{44} in (2) is 138×10^{-7} cm^2/N [15].

4. Fabrication: Both of the sensors were fabricated by bulk micromachining using the standard double side polished *n*-type (100) silicon wafer. The resistivity is 6000–8000 Ω cm and the thickness is 400 μm. The process flow is as follows. (a) Photolithography is employed to pattern the piezoresistors on the front side of the silicon wafer, then SiO_2 layers are grown on both sides of the substrate by thermal oxidation. Then, ion implantation of boron is carried out with a concentration of 3×10^{14} cm^{-3}, forming a sheet resistance of 220 Ω. (b) Heavy born ion diffusion is carried out to consolidate the connections of piezoresistors. (c) The passivation layers of Si_3N_4, SiO_2 are deposited successively by means of low pressure chemical vapour deposition and plasma enhanced chemical vapour deposition. (d) Contacts are then photo patterned and etched on the front side utilising reactive ion etching. To activate the boron ion electrically and make the dopant uniform, annealing technology is executed at 1100°C for 30 min under a nitrogen atmosphere. For the connections of the resistors and formations of the bonding pads, a metallisation process is performed to sputter Au. Ohmic contacts

Table 2 Simulation and calibration results of configurations

	E-type	BMMI		BMQI	
	ANSYS	ANSYS	Experiments	ANSYS	Experiments
U_{fp}, mV/500 Pa	15.066	19.996	17.482	27.301	26.693
U_{fa}, mV/15 g	1.132	1.644	1.448	1.119	1.274
f, Hz	4802.1	6936.6	7375	10833	10275
PF, Hz$^{1/4}$	110.8192	110.9798	111.8827	248.798	210.947
simulation error	/	0.807%	/	17.9432%	/

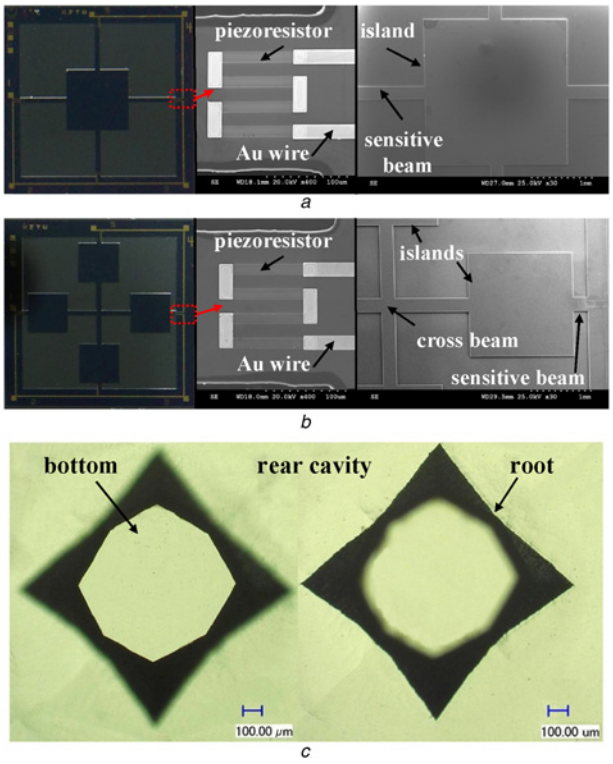

Figure 4 *Photos of the fabricated sensor dies*
a Sensor die and SEM images about BMMI
b Sensor die and SEM images about BMQI
c CCD of the undercut island on the bottom and root planes

between the Au wires and the piezoresistors are reinforced by a sintering process. (e) For creating cavities, forming islands and reducing the height of islands, KOH etching is used on the back side of the wafer after being patterned. The etching is carried out in the pure aqueous KOH solution with a KOH content of 30 wt % at a temperature of 80 ± 1°C, resulting in an etching rate of 1.0 μm/min. (f) Cr is sputtered on the glass acting as anti-adsorption electrodes. The back side of the wafer is attached to Pyrex 7740 glass under vacuum conditions by an anodic bonding process at a temperature of 350°C, under the voltage of 1000 V. (g) Inductively coupled plasma etch is involved to form beams on the front side with an etching rate of 0.6 μm/min. To singulate the arrays of the sensor dies from the wafer, a semiautomatic dicing saw is used along the 400 μm width scribe line marked by a P-doping layer at a feed rate of 2.5 cm/s.

The fabricated sensor dies are shown in Figs. 4*a* and *b*, where SEM images of the two sensor chips are displayed. In addition, the CCD photograph of the undercut island in the rear cavity of BMQI is presented in Fig. 4*c*. The calculated CC undercutting conforms well to the actual fabrication except for some minor difference in the root, which is attributed to the assumption that the fast etching planes are unchanging.

5. Experimental setup: To describe the static characterisation of the sensors, a complete experimental setup was established as shown in Fig. 5*a*. The compressor acts as a pressure source. The sensors were calibrated with a reference pressure monitor (FLUKE A100 K), excited by a 3 V DC power supply (RIGOL DP1116A) and the outputs were measured by a multi-meter (KEITHLEY 2000).

To assess the dynamic performances approximately, another two sensor dies corresponding to BMMI, BMQI with a through-hole on the glass base are utilised. The hole makes the pressures inside and outside the cavity equal, thus the applied atmospheric pressure is equivalent to zero, and the sensor chips are only affected by

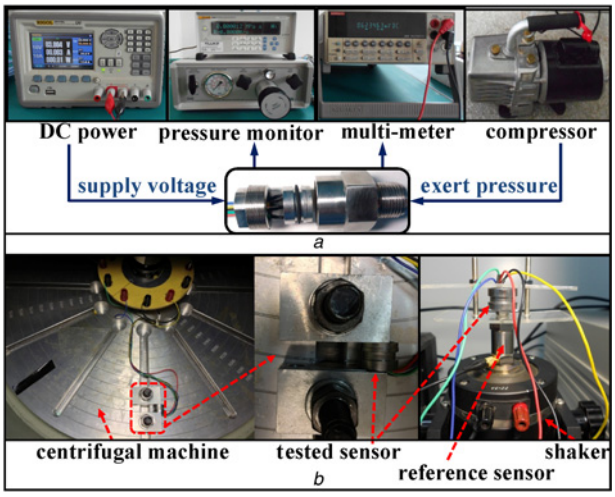

Figure 5 *Static and dynamic calibration system*
a Pressure calibration setup
b Acceleration and resonant frequency calibration setup

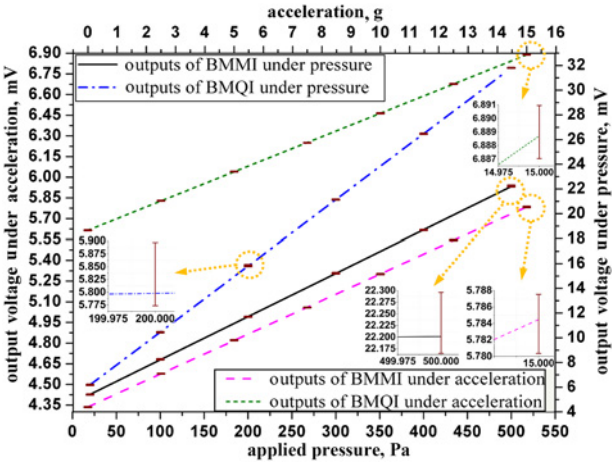

Figure 6 *Experimental results on pressure and acceleration*

vibration acceleration, which was convenient for dynamic experiments. A stable centrifugal machine was used for acceleration calibration along the normal direction of the membrane of the two sensors. Through changing the rational speed, accelerations of up to 15 g with an interval of 2.5 g are imposed.

The natural frequency was evaluated by testing the two sensors with a hole. By fixing one of the two tested sensors and a reference sensor on a shaker, a peak concerning the voltage ratio of these two sensors will be generated when a sine sweep frequency passes through. Both the centrifugal machine and the shaker are shown in Fig. 5*b*.

6. Results and discussion: The pressure and acceleration calibration results are plotted in Fig. 6. The pressure varies from 20 to 500 Pa at room temperature. In the Figure, the calibrated data of the five-round journey are described with different kinds of lines fixed by least-square fitting. The standard errors of the testing points are marked by error bars. The maximum standard errors of BMMI and BMQI are 0.06537, 0.06181 and 0.00359, 0.00196, corresponding to pressure and acceleration, respectively, and they are enlarged in the Figure. In the modal calibration, the peaks induced by the resonance are drawn in Fig. 7. Although slightly different damping factors and minor fabrication variations exist, the acceleration and modal experiments are still significant

doi: 10.1049/mnl.2014.0236

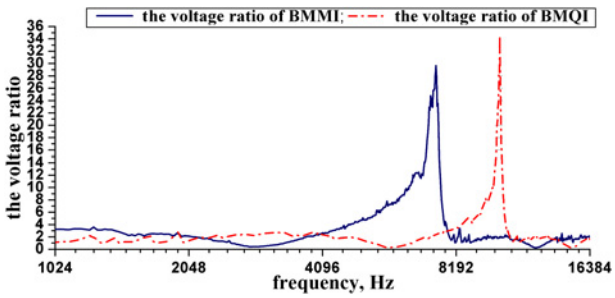

Figure 7 *Modal analysis results*

Table 3 Static characteristics of the sensors

	BMMI	BMQI
output under atmosphere, mV	544.37	1413.3
sensitivity, μV/V/Pa	11.655	17.795
nonlinearity, %FS	0.1966	0.1405
hysteresis, %FS	0.4371	0.2847
repeatability, %FS	2.2374	1.4788
basic accuracy, %FS	2.2881	1.5125

for evaluating the dynamic performances of the sensors under near-vacuum conditions.

The calibration results above are listed in Table 2 for comparing the simulation errors of the PF. In the Table, the full-scale outputs on pressure and acceleration are calculated based on the least-square method. The performance factor PF is derived from (6), and it reveals that the BMQI features the highest comprehensive performance. The PF of BMQI is 88.5% higher than for BMMI. The simulation results show that the sensitivity of BMMI is 32.7% higher than the E-type one, and the natural frequency is 44.4% higher. However, the PF of BMMI has been dragged down to be nearly the same, by the 45.2% higher acceleration interference. The detailed static characteristics of the sensors are listed in Table 3.

7. Conclusion: This work has attempted to explore the assessment of the performance of absolute micropressure sensors considering vibration influences. A performance factor has been proposed to try to reflect the comprehensive performance. To validate the rationality of the defined performance factor, two configurations have been proposed, optimised and actually fabricated. Experimental results have demonstrated that the performance factor is of significance for evaluating the overall property of a sensor.

8. Acknowledgments: This work is supported by the National Science Foundation for Distinguished Young Scholars of China (no. 51325503), the Young Scientists Fund of the National Natural Science Foundation of China (no. 51305336), the National High Technology Research and Development Program of China (863 Program) (no. 2013AA041108), the Program for Changjiang Scholars and Innovative Research Team in University of China (no. IRT1033) and the Postdoctoral Science Foundation of China (no. 2013M532036).

9 References

[1] Guiming Z., Libo Z., Zhuangde J., Shuming Y., Yulong Z., Enze H., *ET AL.*: 'Surface stress-induced deflection of a microcantilever with various widths and overall microcantilever sensitivity enhancement via geometry modification', *J. Phys. D, Appl. Phys.*, 2011, **44**, (42), p. 425402

[2] Mackowiak P., Schiffer M., Xin X., Obermeier E., Ha-Duong N.: 'Design and simulation of ultra high sensitive piezoresistive MEMS sensor with structured membrane for low pressure applications'. 12th Electronics Packaging Technology Conf. (EPTC 2010), Singapore, 2010, pp. 757–761

[3] Tian B., Yulong Z., Zhuangde J., Bin H.: 'The design and analysis of beam-membrane structure sensors for micro-pressure measurement', *Rev. Sci. Instrum.*, 2012, **83**, (4), p. 045003

[4] Gradolph C., Friedberger A., Muller G., Wilde J.: 'Impact of high-g and high vibration environments on piezoresistive pressure sensor performance', *Sens. Actuators A, Phys.*, 2009, **150**, (1), pp. 69–77

[5] Lin L., Chu H.-C., Lu Y.-W.: 'A simulation program for the sensitivity and linearity of piezoresistive pressure sensors', *J. Microelectromech. Syst.*, 1999, **8**, (4), pp. 514–522

[6] Shimazoe M., Matsuoka Y., Yasukawa A., Tanabe M.: 'A special silicon diaphragm pressure sensor with high output and high-accuracy', *Sens. Actuators*, 1982, **2**, (3), pp. 275–282

[7] Bao M.H., Yu L.Z., Wang Y.: 'Micromachined beam-diaphragm structure improves performances of pressure transducer', *Sens. Actuators A, Phys.*, 1990, **21**, (1–3), pp. 137–141

[8] Johnson R.H., Karbassi S., Sridhar U., Speldrich B.: 'A high-sensitivity ribbed and bossed pressure transducer', *Sens. Actuators A, Phys.*, 1992, **35**, (2), pp. 93–99

[9] Quan W., Jianning D., Wenxiang W.: 'Fabrication and temperature coefficient compensation technology of low cost high temperature pressure sensor', *Sens. Actuators A, Phys.*, 2005, **120**, (2), pp. 468–473

[10] Clark S.K., Wise K.D.: 'Pressure sensitivity in anisotropically etched thin diaphragm pressure sensors', *IEEE Trans. Electron Devices*, 1979, **26**, (12), pp. 1887–1896

[11] Young W.C.: 'Roark's formulas for stress and strain' (McGraw-Hill, New York, 1986, 6th edn), pp. 440–464

[12] Hopcroft M.A., Nix W.D., Kenny T.W.: 'What is the Young's modulus of silicon?', *J. Microelectromech. Syst.*, 2010, **19**, (2), pp. 229–238

[13] Timoshenko S., Woinosky-Krieger S.: 'Theory of plates and shells' (McGraw Hill Classic Textbook, New York, 1987, 2nd edn)

[14] Fan W., Zhang D.C.: 'A simple approach to convex corner compensation in anisotropic KOH etching on a (100) silicon wafer', *J. Micromech. Microeng.*, 2006, **16**, (10), pp. 1951–1957

[15] Tufte O.N., Stelzer E.L.: 'Piezoresistive properties of silicon diffused layers', *J. Appl. Phys.*, 1963, **34**, (2), pp. 313–318